Structure and energetics of Er defects in $LiNbO_3$ from first-principles and thermodynamic calculations

Haixuan Xu (徐海譞),[1] Donghwa Lee (이동화),[1] Susan B. Sinnott,[1] Venkatraman Gopalan,[2] Volkmar Dierolf,[3] and Simon R. Phillpot[1,*]

[1]*Department of Materials Science and Engineering, University of Florida, Gainesville, Florida 32611, USA*

[2]*Department of Materials Science and Engineering, Pennsylvania State University, University Park, Pennsylvania 16802, USA*

[3]*Department of Physics, Lehigh University, Bethlehem, Pennsylvania 18015, USA*

(Received 22 June 2009; revised manuscript received 7 September 2009; published 8 October 2009)

The effects of Er defects on the structure and energetics of $LiNbO_3$ are determined using electronic-structure calculations at the level of density-functional theory combined with thermodynamic calculations. It is found that under both Li_2O-rich and Nb_2O_5-rich conditions, Er^{3+} sits on the Li site and is displaced along the uniaxial direction of the hexagonal structure toward the vacant cation site. The charge compensation mechanism is predicted to be lithium vacancies under Nb_2O_5-rich conditions, consistent with a previous conjecture; charge compensation is predicted to be by Er^{3+} on a Nb site under Li_2O-rich conditions. It is also found that low concentration of lithium vacancies could significantly affect the defect chemistry: when a Li-poor congruent sample is converted to the stoichiometric, there may be a negligible concentration of Er on Nb sites. The diffusivity and average diffusion distance under annealing of defects are also discussed.

DOI: 10.1103/PhysRevB.80.144104 PACS number(s): 61.72.−y, 71.15.Mb, 71.20.Nr, 71.27.+a

I. INTRODUCTION

$LiNbO_3$ is an versatile material due to its ferroelectric, piezoelectric, photorefractive, and electro-optical properties with applications in modulators, wavelength filters, second-harmonic generators, and nonvolatile memories.[1,2] During the past decades, there have been a number of studies of Er-doped $LiNbO_3$ (Refs. 3–8) for optical lasers, optical amplifiers, and integrated optical circuits.[9–12] Furthermore, Er^{3+} ions have been employed as a probe to investigate the structure of domain walls and defect/domain-wall interactions.[13–15] Various experimental techniques, including electron-spin resonance,[4] x-ray standing-wave (XSW) analysis ,[16,17] Rutherford backscattering,[18] extended x-ray absorption fine structure (EXAFS),[19] and ion-beam channeling,[20] have been employed to investigate the site selectivity of Er^{3+}. Moreover, several optical and magnetic-resonance spectroscopy studies[3,6,21–23] have been used to determine the local environments and configurations around the $Er_{Li}^{\cdot}$ sites. While some of these studies used congruent $LiNbO_3$ samples grown by the Czochralski method,[24,25] others used stoichiometric $LiNbO_3$ produced through vapor transport equilibration (VTE) (Refs. 26–28) from congruent samples. The influence of the sample stoichiometry on the site selectivity and distribution is unknown, which makes the comparison between experiments on samples from different synthesis technique problematic. In addition to understanding how the Er^{3+} ions are incorporated into the structure, an understanding of the associated charge compensation mechanisms is also necessary.

Atomic-level simulations[29] at 0 K using an empirical potential predicted the dominant defect to be $Er_{Li}^{\cdot}$ compensated by Er_{Nb}''. However, at room temperature, the simulations predicted that Er^{3+} ions occupy the Nb site, compensated by $Nb_{Li}^{\cdot\cdot\cdot\cdot}$. It is not clear how such a small temperature change (300 K=0.026 eV) could cause such a qualitative change in the dominant crystal defect. The experimental and theoretical results thus indicate that the charge compensation mechanism for Er in $LiNbO_3$ is still not well understood.

In the present study, electronic-structure calculations at the level of density-functional theory (DFT) combined with thermodynamic calculations are employed to determine the defect site selectivity of Er^{3+} in $LiNbO_3$ and the corresponding charge compensation mechanisms under various conditions. In particular, the defect formation energies (DFEs) of various possible single defects are calculated. The dependence of the DFEs on the position of the Fermi level is established. The formation energies of defect clusters are then predicted based on the sum of the DFEs of isolated point defects. The association energies, resulting from the elastic and electrostatic interactions among the constituents of a defect cluster, are explicitly determined by simulating entire defect clusters in one supercell. The dominant defect complexes are predicted based on their stability under different conditions and the simulation results are assessed in the context of the current experimental understanding.

II. METHODOLOGY

A. DFT calculations

The DFT (Refs. 30 and 31) calculations are carried out in the Vienna *ab initio* Simulation Package (VASP) (Refs. 32 and 33) at the level of the generalized gradient approximation (GGA). The projected augmented wave (PAW) method[34] is used to achieve maximum accuracy[35] while maintaining the flexibility of the pseudopotential approach.[36] The cutoff energy for the plane-wave basis set is chosen to be 400 eV based on convergence tests.[37] The system size is $2\times2\times2$ unit cells (each of 30 atoms), which for perfect $LiNbO_3$ contains 240 atoms and 1440 electrons; periodic boundary conditions are applied in all three dimensions. The integration over the Brillouin zone uses a $4\times4\times2$ Monkhorst-Pack[38] k-point mesh. This mesh is chosen because the length of the

uniaxial c axis is approximately twice that of the a axis. The structure is optimized to within an error of 0.01 eV.

The Li $2s^1$, Nb $4p^6 4d^4 5s^1$, and O $2s^2 2p^4$ valence electrons are treated explicitly. The electronic structure of Er is [Xe] $4f^{12}6s^2$. Due to the localized nature of $4f$ electrons,[39,40] the frozen-core approximation[41,42] is used. In VASP, 11 of 12 f electrons are treated as the frozen core, with only a single f electron treated as a valence electron.[43] In addition, the $6s^2$ and $5p^6$ are also treated as valence electrons, resulting in a total of nine Er valence electrons.

The localized nature of $4f$ electrons results in strong correlation effects. In general, mean-field theories, such as the local-density approximation (LDA) and GGA, cannot accurately describe the strong correlations of d and f electrons.[43–45] Therefore, in addressing this problem, either high level theory or a correction to LDA or GGA, such as DFT+U approach,[46,47] is required. In this work, both the GGA and GGA+U methods have been used. The effect of the +U term on defect energetics is assessed.

B. DFE

The supercell method[48–50] is used to calculate the defect formation energies of both isolated defects and defect clusters. The DFE of a defect or defects, denoted as α, with charge state q is defined as[51]

$$\Delta E_f(\alpha,q,T,P) = E^{\text{total}}(\alpha,q) - E^{\text{total}}(\text{perfect}) + \sum_i n_i\mu_i - q(\varepsilon_F + E_v + \Delta V), \quad (1)$$

where α is the defect type, q is the charge of the defect(s), T is temperature, and P is partial pressure of oxygen. $E^{\text{total}}(\alpha,q)$ is the total energy obtained from DFT calculation of a supercell with the defect(s); E^{total}(perfect) is the total energy of the supercell without any defects. n_i is the number of ions of species i that have been added to or removed from the supercell when the defects are created; μ_i is the chemical potential of element i. ε_F is the Fermi level with respect to the valence-band maximum (VBM) in the bulk single crystal. E_v is the VBM of the bulk system. ΔV is the difference in the electrostatic potentials between the defected and undefected systems.[51]

In principle, the free energy rather than the total energy should be used in Eq. (1) for the calculation of the DFEs. However, the total internal energy of a supercell calculated with DFT corresponds to the Helmholtz free energy at zero temperature, neglecting zero-point vibrations.[52] These calculations thus neglect the contributions from the vibrational entropy; fortunately, experimental and theoretical results for entropies of point defects typically fall between 0 and $10k$, where k is the Boltzmann constant.[51] Detailed analyses by Kohan *et al.*[53] for ZnO and by He *et al.*[54] for TiO_2 concluded that entropic effects can be neglected. Consequently, the neglect of the entropy term here will not qualitatively change our conclusions.

C. Thermodynamic framework

The same methodology for the chemical potential is used here as in our previous study[55] of intrinsic defects. The chemical potential of each element has to satisfy the constraint that $LiNbO_3$ be stable against decomposition to metallic Li or Nb and to decomposition to the constituent oxides: Li_2O and Nb_2O_5. Experimentally, the oxygen chemical potential can be changed through the temperature and/or oxygen partial pressure. There are two limits on the oxygen chemical potential in $LiNbO_3$, corresponding to extremely oxidizing conditions or extremely reducing conditions. These constraints would actually result in unrealistically high and low oxygen partial pressures, respectively, with the physically attainable range of partial pressures being much narrower.

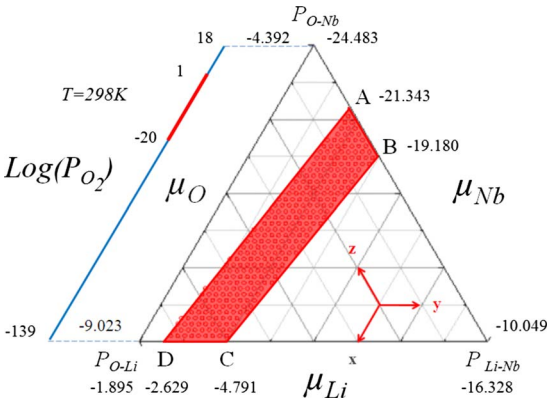

FIG. 1. (Color online) Stability range of chemical potentials (in eV) of the elements in $LiNbO_3$. The region enclosed by points A, D, and $P_{\text{Li-Nb}}$ satisfies the condition that the material does not decompose into Li_2O, while the region enclosed by points B, C, $P_{\text{O-Li}}$, and $P_{\text{O-Nb}}$ satisfies the condition that the material does not decompose into Nb_2O_5. The intersection of these two regions defines the thermodynamically allowable range of chemical potentials. This stability region is thus defined by the shaded quadrilateral enclosed by the points A, B, C, and D. Line AD represents using Li_2O as reference state; line BC represents using Nb_2O_5 as reference. The oxygen partial pressure range (in atm) is that for room temperature.

Bringing all of the stability criteria together, we constructed the ternary chemical-potential map shown in Fig. 1, where the points in chemical-potential space should be analyzed in a manner analogous to that for the composition in a conventional ternary phase diagram.[56] The details of the construction procedure of this map can be found in our previous study,[55] along with a full explanation of each point and line. Two scenarios are most relevant. Under Li_2O-rich conditions, for which Li_2O is the reference state, the composition-weighted sum of the lithium and oxygen chemical potentials is equal to the total energy of Li_2O, which is line AD in Fig. 1. Nb_2O_5-rich conditions, for which Nb_2O_5 is the reference state, correspond to the line BC in Fig. 1.

A physical manifestation of Li_2O-rich conditions is the conversion of congruent samples to nearly stoichiometric $LiNbO_3$ using VTE, which takes place in a Li_2O vapor.[26–28] Nb_2O_5-rich conditions correspond to growth under a Nb_2O_5 vapor or, more generally, the condition that the constitutive sum of chemical-potential value of Nb and O are close to that of Nb_2O_5. Congruent $LiNbO_3$ is grown by the Czochralski process in air rather than in Nb_2O_5 vapor. However, based on structural analysis, the local bonding environments

of Nb and O in $LiNbO_3$ are very similar to that in Nb_2O_5. Therefore, it is assumed here that the congruent melting condition can be analyzed as if it were grown under Nb_2O_5-rich conditions, i.e., for the Nb_2O_5 reference state.

The chemical potential of Er is an important unknown quantity that determines *absolute* values for defect energies. Possible choices for the reference state include the pure metal and the binary oxide. Here, the chemical potential of Er in $LiNbO_3$ is assumed to be the same as that in Er_2O_3, which has a very similar bonding environment to that of Er in $LiNbO_3$. In particular, Er_2O_3 has a bixbyite structure with space group $Ia3$.[57,58] The Er ions in Er_2O_3 are all six-coordinated, with two different crystallographic positions. The average length of the bond is calculated to be 2.266 Å using DFT-GGA. In $LiNbO_3$, Er ions are also six-coordinated and have average Er-O bond lengths of 2.243 Å.[55]

All of the defect structures discussed in the literature and considered here involve two Er ions. Thus, since its value affects all formation energies equally, the value of the chemical potential of Er is irrelevant for determining the *relative* stability of these defect structures.

III. DFES OF ER IN $LiNbO_3$

The current paper focuses on the following four extrinsic defect clusters that have been discussed in the literature: $2Er_{Li}^{\cdot\cdot}+4V_{Li}^{\prime}=2(Er_{Li}^{\cdot\cdot}+2V_{Li}^{\prime})$, $Er_{Li}^{\cdot\cdot}+Er_{Nb}^{\prime\prime}$, $2Er_{Li}^{\cdot\cdot}+Nb_{Li}^{\cdot\cdot\cdot\cdot}$, and $2Nb_{Li}^{\cdot\cdot\cdot\cdot}+4V_{Li}^{\prime}+2Er_{Nb}^{\prime\prime}$.[2,29] Two completely separated $Er_{Li}^{\cdot\cdot}+2V_{Li}^{\prime}$ clusters are considered because this approach allows all of the defect clusters to be analyzed independently of the chemical potential of the Er.

While the above defect structures are written in terms of fully charged constituent defects, partially charged and charge-neutral defects are also possible.[51] For example, many experiments on TiO_2 have concluded that as the oxygen partial pressure decreases from moderately reducing to extremely reducing conditions, there is a transition from a fully charged oxygen vacancy to a singly charged oxygen vacancy or triply charged titanium interstitial.[54] Thus, before characterizing the defect clusters, it is important to analyze the individual defects with various charge states. The following sections will discuss the results obtained for individual defects of various charges, followed by the defect clusters. For the defect clusters, the constraint of charge neutrality leads to the simplification of not having to consider the effects of the location of the Fermi energy.[55]

A. Single defects

Here, simulations of single isolated defects in the $2\times2\times2$ supercell are analyzed, which corresponds to the situation of the charge-compensating defects being far from both the Er defect and each other. The DFEs of Er_{Li} and Er_{Nb} defects with various charge states in $LiNbO_3$ have been calculated using Eq. (1). The influence of the Fermi energy on the stability of each individual defect is considered. The reference zero of the Fermi energy is assigned to be the VBM of the perfect structure; the highest Fermi energy thus corresponds to the conduction-band minimum (CBM), which for GGA is 3.5 eV, close to the experimental value of 3.78 eV for the band gap.[59,60] A Fermi energy at the center of the gap corresponds to the pure system, while *p*-type and *n*-type correspond to Fermi energies closer to the valence and the conduction bands, respectively.[61] As the Fermi level could shift in the presence of impurities and defects, two extreme cases correspond to $\varepsilon_f=0$ and $\varepsilon_f=3.5$ are discussed.

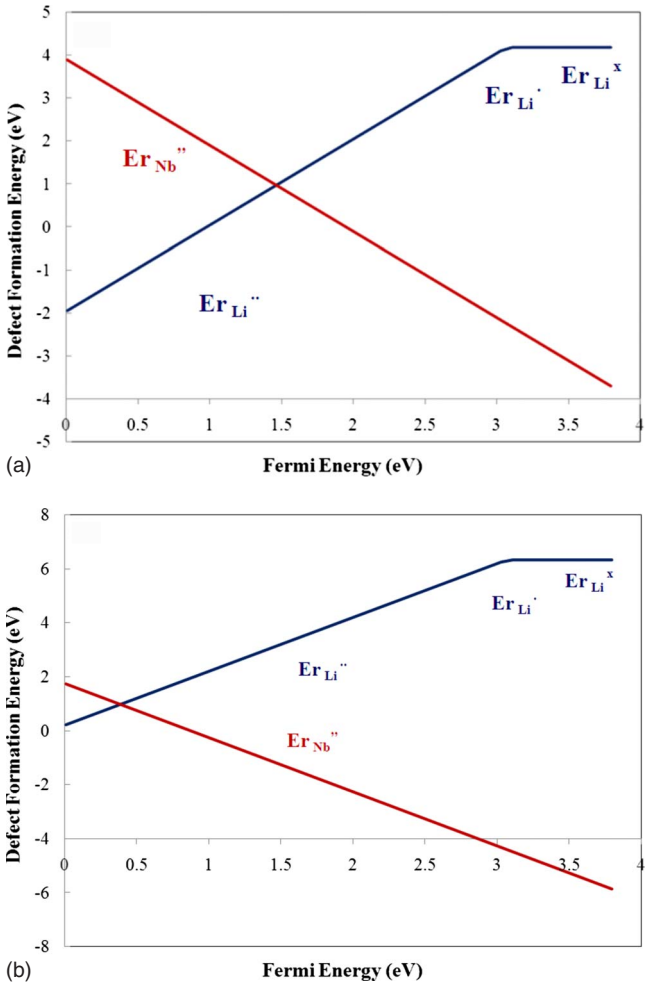

FIG. 2. (Color online) Defect formation energies of the lowest-energy charge state of Er_{Li} and Er_{Nb} as a function of Fermi energy; the lowest-energy charge state is given in each case. The Fermi energy ranges from $E_F=0$ (left) at the VBM to $E_F=3.5$ eV at the conduction-band minimum (right). (a) using Nb_2O_5 as reference state. (b) using Li_2O as reference state.

The dependence of DFEs on the Fermi level is shown in Fig. 2 using Nb_2O_5 (the BC line in Fig. 1) as the reference state. At each value of the Fermi level, Fig. 2 includes only the charge state with the lowest DFE of each individual defect. The slopes of the lines in Fig. 2 represent the charge states of the defects [see Eq. (1)]. As the Fermi energy increases, the thermodynamically stable charge of the Er_{Li} decreases. $Er_{Li}^{\cdot\cdot}$ has a lower energy than its singly charged counterpart $Er_{Li}^{\cdot}$ for most of the range of Fermi level, while $Er_{Nb}^{\prime\prime}$ has the lowest DFE throughout the entire range. The partial densities of states of Li, Nb, O, and Er for $Er_{Li}^{\cdot\cdot}$ and $Er_{Nb}^{\prime\prime}$ have been also generated and given in Fig. 3. No significant effect

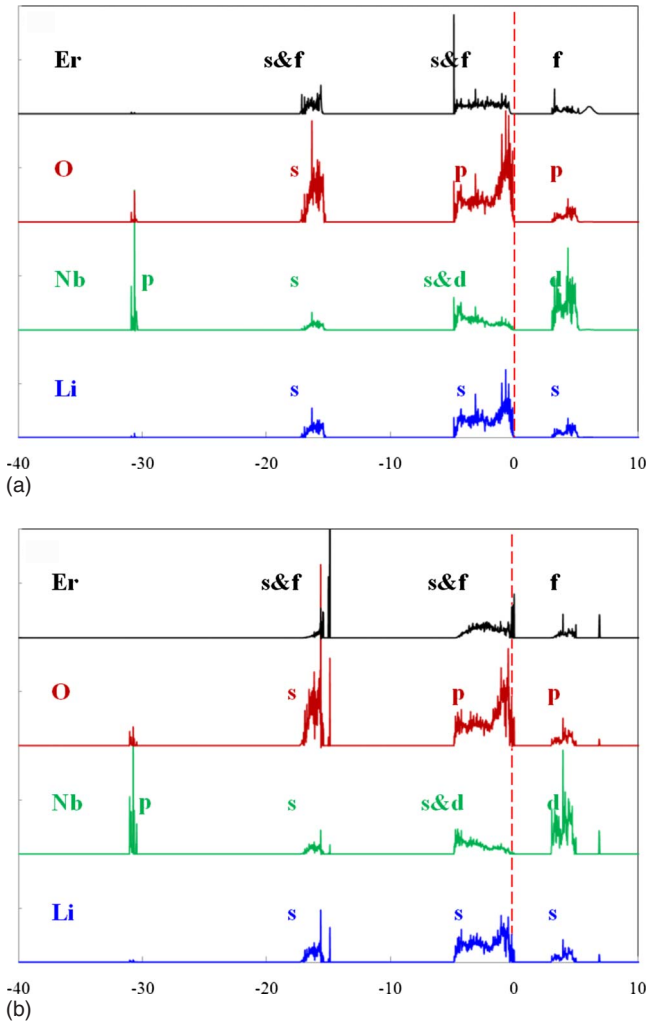

FIG. 3. (Color online) (a) PDOS for $Er_{Li}^{\cdot\cdot\cdot}$; (b) PDOS for Er_{Nb}''. The absolute values of the number of the DOS in the two figures have been rescaled to make the comparison easier.

of Er on the partial density of state (PDOS) of lithium, niobium, and oxygen is observed. From Fig. 3, it can be seen that there is a greater overlap in the PDOS of the Er_{Nb} and O ions compared with Er_{Nb}'' and O, indicating stronger covalent bonding.

In the unit cell of $LiNbO_3$, six closed-packed planes are stacked.[2] The cations lie in the oxygen octahedral in repeating sequence: Li, Nb, vacant site, Li Nb, vacant site….[2] Within a single plane of cations, there is an ordered arrangement of Li ions, Nb ions, and vacant sites. For $Er_{Li}^{\cdot\cdot\cdot}$, the DFT calculations show that the Er is shifted along ⟨0001⟩ toward the vacant site by ~0.17 Å. The observation by Gog *et al.* using XSW spectroscopy[16,17] showed the Er to be in a position near a Li site, but displaced normal to the basal plane by 0.46 Å.[16] This difference between the experimental measurement and calculated value for the displacement may have several origins. First, the experiments were performed using congruent $LiNbO_3$, while the simulations were carried out for stoichiometric material. Second, the experiments measured the near-surface region where Er is incorporated through diffusion, while the calculations are for the bulk.

TABLE I. Defect formation energies for defect reactions under different reference states. The chemical potential of Er is assumed to be the same as the value in Er_2O_3. These values are calculated based on the single defect energy without considering association effects.

	DFE (eV)	
Defect reaction fully charged	Li_2O	Nb_2O_5
$2Er_{Li}^{\cdot\cdot\cdot}+4V_{Li}'$	8.369	–4.607
$Er_{Li}^{\cdot\cdot\cdot}+Er_{Nb}''$	1.939	1.939
$2Er_{Li}^{\cdot\cdot\cdot}+Nb_{Li}^{\cdot\cdot\cdot\cdot}$	4.274	4.274
$2Er_{Nb}''+4V_{Li}'+2Nb_{Li}^{\cdot\cdot\cdot\cdot}$	13.039	0.064

Both the composition and surface effects could cause a change in the position of the Er ions. Third, the difference may be also due to the limitation of the current calculation method, which simulates the defects in a finite-size supercell and assumes that the defect concentration is in the dilute limit. For partial charged defects, $Er_{Li}^{\cdot\cdot\cdot}$ and Er_{Li}^{x}, the displacements are 0.14 and 0.08 Å, respectively. By comparison, the DFT calculations for Er_{Nb}'' yield a displacement of only ~0.02 Å toward the vacant site. The displacements for Er_{Nb}' and Er_{Nb}^{x} are less than 0.005 Å.

These results are readily understood in terms of the electrostatic and elastic interactions within the system. Thus, when Er substitutes on a Li site, the repulsive electrostatic interaction between Nb and Er is greater than that between Nb and Li and thus forces the Er toward the vacancy. The ionic radii of Li^+, Nb^{5+}, and Er^{3+} are 0.76, 0.64, and 0.89 Å, respectively.[62] Therefore, the larger size of the Er ion also tends to push it closer to the vacanct site thus both interactions push the Er toward the vacant site. By contrast, when Er substitutes on a Nb site, the smaller Er charge leads to weaker repulsion from the Li, thus tending to move the Er ion away from the vacant site. However, the larger ionic radii will again push the Er toward the vacant site. The electrostatic and elastic interactions thus tend to counteract each other, resulting in only a small net displacement.

B. Defect complexes

The energies of neutral defect complexes are first determined from the formation energies of the individual defects (Table I). As mentioned above, because these defects are charge neutral, their energies are independent of the location of the Fermi level. However, the DFEs of the clusters do depend on the choice of reference state. From Fig. 4, it can be seen that the formation energies of the $Er_{Li}^{\cdot\cdot\cdot}+Er_{Nb}''$ and $2Er_{Li}^{\cdot\cdot\cdot}+Nb_{Li}^{\cdot\cdot\cdot\cdot}$ clusters are independent of the reference state. This is because within $LiNbO_3$, the sum of chemical potentials of Li and Nb is constant for any given value of the chemical potential for oxygen. By contrast, the DFEs of the $2Er_{Li}^{\cdot\cdot\cdot}+4V_{Li}'$ and $2Er_{Nb}''+4V_{Li}'+2Nb_{Li}^{\cdot\cdot\cdot\cdot}$ clusters do depend on the reference state of chemical potential.

The calculations show that the formation energy for $2Er_{Li}^{\cdot\cdot\cdot}+4V_{Li}'$ is negative for the Nb_2O_5 reference state. This

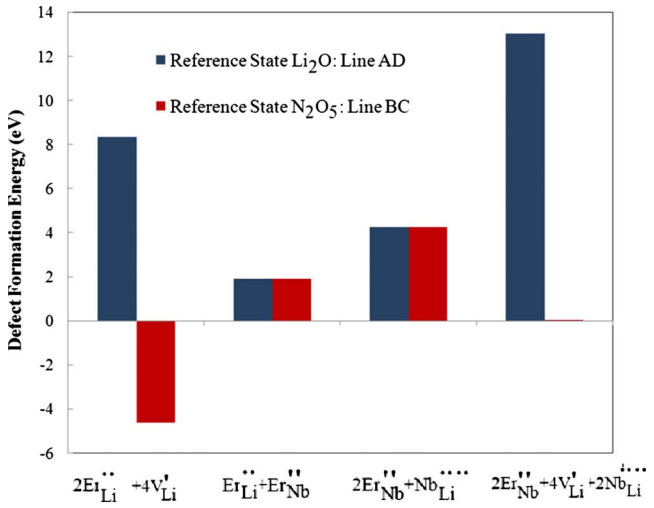

FIG. 4. (Color online) Formation energies of Er-related defect clusters under Li_2O-rich conditions (blue) and Nb_2O_5-rich conditions (red).

result is similar to the previously studied intrinsic $Nb_{Li}^{\cdot\cdot\cdot\cdot}+4V_{Li}^{'}$ cluster, which also showed a negative DFE, indicating that these defect clusters will spontaneously form under these conditions. Negative formation energies lead to the apparent contradiction that their concentration should increase indefinitely, a physically unreasonable result. The resolution is that the calculation was performed in the dilute limit and that it can safely be presumed that the DFEs will increase with increasing concentration such that the concentration of the defect clusters remains bounded and the system remains stable. Under Nb_2O_5-rich conditions, the $2Er_{Nb}^{''}+4V_{Li}^{'}+2Nb_{Li}^{\cdot\cdot\cdot\cdot}$ cluster has a very small positive formation energy and might thus be expected to also be observed. The calculations also predict that for the Li_2O reference state, $Er_{Li}^{\cdot\cdot}+Er_{Nb}^{''}$ has the lowest DFE. However, the DFE is positive, which indicates energy is required to create the defects under conditions such as VTE. Based on the thermodynamic calculation, the concentration of such defects at room temperature is very low. This point is discussed in detail Sec. IV (iv).

To this point, the calculations have assumed that the individual defects that form a defect cluster are infinitely far away from each other; that is, there are no interactions between them. However, due to the charge and elastic interactions induced by the differences in ionic radii, defect association can be expected to change the DFEs. Here, the case of $Er_{Li}^{\cdot\cdot}+2V_{Li}^{'}$ is analyzed. While there are an almost innumerable number of possible different compensating structures, it is only necessary to analyze the limiting case of association, in which some of the compensating vacancies are in the first-neighbor shell while all of the others are far from the Er defect. Cases in which vacancies lie in the second or third shell or beyond can be assumed to have lower association energies. There are six Li sites in the first nearest-neighbor (FNN) shell around the Er-occupied Li site, as indicated in Fig. 5. The arrangement of the Li vacancies can conveniently be divided into three categories:

(i) A0: No lithium vacancies in the FNN shell;

(ii) A1: One lithium vacancy in the FNN shell;

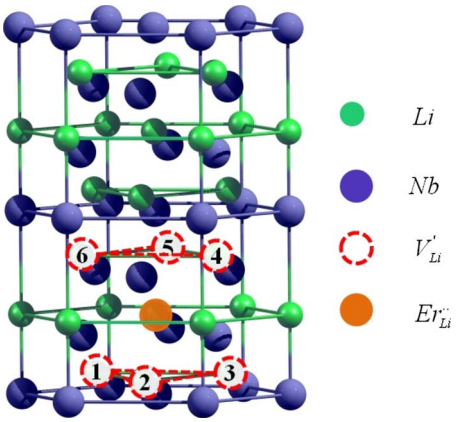

FIG. 5. (Color online) Possible lithium vacancy positions in the FNN around Er sitting on lithium site. The oxygen sublattice is not shown.

(iii) A2: Two lithium vacancies in the FNN shell.

In the A0 structure, there is no association of the vacancies; this is the case analyzed above and found to have negative formation energy for the Nb_2O_5 reference state. For A1, there are two distinct configurations for one lithium vacancy sitting around the Er site. The lithium vacancy could lie above the Er ion (4, 5, or 6 in Fig. 5) or below the Er ion (1, 2, or 3 in Fig. 5). For the A2 case, there are $C_6^2=15$ possible configurations of vacancies. However, due to the threefold rotational symmetry around the $Er_{Li}^{\cdot\cdot}$, only four of these configurations are crystallographically distinct. The four different arrangements are 1–2, 1–4, 4–5, and 2–5 in Fig. 5.

As illustrated in Fig. 6, the energy of the A1 structure is lower than for the A0 structure, while the energy of the A2 structures are lower yet by 0.068 eV/defect (i.e., −0.204 eV for the total cluster). These results indicate an attractive interaction between $Er_{Li}^{\cdot\cdot}$ and $V_{Li}^{'}$, which is consistent with the conjecture of Dierolf *et al.*[8] that $Er_{Li}^{\cdot\cdot}$ is compensated by a $V_{Li}^{'}$ close to $Er_{Li}^{\cdot\cdot}$.

Since this association energy is relatively small, it might be supposed that the structure of a defect cluster could fluctuate dynamically among various symmetry equivalent con-

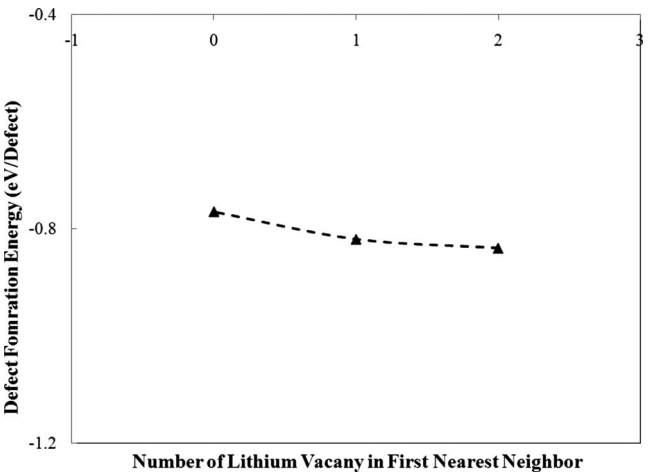

FIG. 6. Defect formation energy for $Er_{Li}^{\cdot\cdot}+2V_{Li}^{'}$ shows the effects of association of the lithium vacancies around $Er_{Li}^{\cdot\cdot}$ site.

figurations. However, our DFT calculations show that the migration barrier for the diffusion of a lithium vacancy between the first nearest neighbor in the lithium sublattice is 1.63 eV, which is consistent with the experimental values of 1.55 eV (Ref. 63) and 1.62 eV (Ref. 64) for the ionic conductivity. These values of activation energies indicate that the transitions among configurations are relatively difficult. However, a lithium vacancy can still move a considerable distance during long-time annealing. For example, experimentally stoichiometric $LiNbO_3$ has been annealed at 250 °C for 5 h.[8] It is assumed that the vibration energy $h\nu_0$ is equal to the thermal energy k_BT.[65] The jump distance between first nearest neighbors is 3.771 Å. Under such condition, the diffusivity of lithium vacancy is calculated to be 3.08×10^{-18} cm^2/s, which compares reasonably well to previous estimates of 5.97×10^{-16} cm^2/s (Mehta *et al.*[63]) and 4.46×10^{-17} cm^2/s (Halstead[64]). The average diffusion distance can then be calculated using the following equation:

$$x=\sqrt{6Dt}, \tag{2}$$

where x is the average diffusion distance, D is the diffusivity, and t is the diffusion time. Using the above value of diffusivity, the average diffusion distances are 8.7 nm (this work), 80.3 nm (Mehta *et al.*[63]), and 21.9 nm (Halstead[64]). The average diffusion distance in the order of tens of nanometers indicates the lithium vacancy can still travel and change the configurations of the defect complex. The calculation is in agreement with the experimental observation that the relative peak emission intensities are modified by the annealing of the sample.[8]

C. Effect of electron localization: GGA+U

To this point, the calculations have been carried out within GGA. To investigate the electron localization and correlation effects, the GGA+U approach is also used for which reasonable values for the U and J parameters are needed. In particular, Dudarev's approach[46] has been used, in which only the difference between U and J is meaningful. Unfortunately, no parameters have been determined for Er in either $LiNbO_3$ or Er_2O_3. However, there are several sets of parameters available for Er in GaN or in $Er_xGa_{1-x}N$.[66,67] For Er in GaN using the density functional based tight-banding (DFT-TB) method,[66] $U-J=10.3$ eV was used. However, it is known that the DFT-TB method yields higher estimates for U and J than does regular DFT.[66] For $Er_xGa_{1-x}N$ using LSDA+U,[67] $U=8.6$ eV and $J=0.75$ eV has been used. Since there are no accepted values for U and J for $LiNbO_3$, we have explored a range in order to map out the possible magnitude of the effects of electron localization: (i) $U-J=4$ eV; (ii) $U-J=7.85$ eV,[67] and (iii) $U-J=10.3$ eV.[66] Although none of these parameters may actually be the best physical representation of electron localization for Er in $LiNbO_3$, they do span the range of reasonable values and should thus enable us to assess the importance of the localization of electrons on its effects on the defect energetics. Because the GGA+U has to be used for both the reference state Er_2O_3 and for Er in $LiNbO_3$, its effects on Er_2O_3 are discussed first, followed by its effects of Er in $LiNbO_3$.

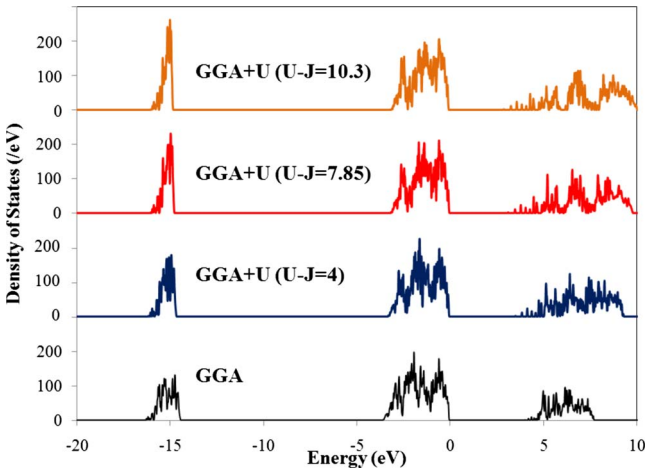

FIG. 7. (Color online) Electronic density of States of Er_2O_3 calculated using GGA and GGA+U. The parameters $U-J=4$ eV, $U-J=7.85$ eV, and $U-J=10.3$ eV are considered.

For Er_2O_3, the band gap calculated using pure GGA is 4.37 eV, which is about 13% less than the experimental value of ~5 eV.[68] This agreement can be considered to be good because it is well known that for many systems, GGA fails to predict the band gap of a material with partially filled d or f orbital.[43–45] There is no significant change in the band gap or electronic density of states for any of the parameter sets for U-J, which indicates that the Er is reasonably described by GGA (Fig. 7).

For Er in $LiNbO_3$, the representative case of $Er_{Li}^{\cdot\cdot}+2V_{Li}'$ is chosen to illustrate the effects of +U, in which the association effect is also considered. For $U-J=4$ eV, $U-J=7.85$ eV, and $U-J=10.3$ eV, the DFE increases by 0.067eV/defect, 0.102 eV/defect, and 0.072 eV/defect, respectively. Thus the stability order predicted from the GGA calculations is correct and the energy values can be considered reliable to within ~0.1 eV/defect. We thus conclude that electron localization as captured by the +U term has no significant effect on either the electronic structure or the defect energetics for these systems.

IV. RELATIONS TO EXPERIMENTS

The principle conclusions of this work are that (i) the Er dopant sits on the Li sites, (ii) various slightly different microstructural configurations of Er sites exist,[8] and (iii) charge compensation is provided by Li vacancies for Li_2O-rich conditions or (iv) by Er on Nb sites under Nb_2O_5-rich conditions. We briefly examine the experimental evidence relevant to each of these predictions.

(i) XSW studies[16,17] found that Er occupies a Li site with C3 point symmetry, but that it is shifted from the ferroelectric Li position by 0.46 Å along the uniaxial direction of the hexagonal structure. Electron spin resonance (ESR) (Ref. 4) identified a single site for Er^{3+} ions, but could not distinguish whether it is Li site or Nb site. Rutherford backscattering[18] and EXAFS (Ref. 19) also yielded Er^{3+} substituting for Li ions, while ion-beam channeling[20] indicated that Er may occupy both Li and Nb sites. The DFT calculations predicted

that Er primarily sits on the Li site under both Li_2O-rich and Nb_2O_5-rich conditions, but with different concentrations based on the difference values of the DFEs. The site is predicted to be shifted along the $-Z$ direction by 0.17 Å. This is consistent with the experimental data measured using XSW and EXAFS which show Er occupies the Li site and moves along $-Z$ direction. However, the magnitude of the displacement is quite different. Possible reasons for this are discussed in Sec. III A. The case of Er site on both Li and Nb sites, which are relevant to ion-beam channeling, is discussed in (iv).

(ii) Optical and magnetic-resonance spectroscopy revealed multiple slightly different sites for the Er ion.[8,69] Baumann *et al.* using XSW and optical spectroscopy[6] found that there are four energetically distinguishable sites for Er, resulting from different local environments. Gill *et al.*[3,22] using total site selective spectroscopy reported six different sites. Furthermore, Dierolf and Sandmann,[8] by combining excitation emission spectroscopy (CEES) as well as absorption, emission, and Raman spectroscopy, found a large number(>11) of different Er^{3+} sites. Moreover, the results of Dierolf and Sandmann[8] suggested that the charge compensation can be classified into two categories: a first close compensation which influences the local symmetry of the Er defect and a secondary compensation probably somewhat further away which influences the local electric field along the z axis. The inclusion of a second more distant charge-compensating Li vacancy further increases the number of potential sites as well. These different arrangements are associated with different local and distant charge compensation species. A2 arrangements (see Sec. III B) are considered as the first category while A1 and A0 fall into the second category. The experimental structure analysis supports there being many slightly different sites for Er^{3+}. When considering only lithium vacancies around the Er^{3+} site, seven different configurations could be identified using DFT calculations. If the presence of impurities, niobium antisites, Er-Er cluster, or even domain walls were to be considered, the number of different Er^{3+} site would be considerably larger. The optical spectroscopy measurements show that the relative number of differently charged compensated Er ions depends on the stoichiometry of the sample. While in congruent samples, the more perturbed A2-type arrangements dominate; in stoichiometric samples, the less perturbed arrangements are more prominent. Furthermore, under domain inversion at room temperature during which the charge-compensating defects are immobile, drastic changes are observed for some defect configurations and no changes are observed for others. In particular, the majority defect configuration in stoichiometric samples remains unchanged (aside from a small spectral shift). For this reason, it is likely that this defect has distant charge compensation as described by configuration A0.

(iii) A consensus as to the precise nature of the charge compensation mechanism for $Er_{Li}^{\cdot}$ has not yet been achieved. It has been reported by Gill *et al.*[22] that the site redistribution associated with an increase in Er concentration is very similar to that associated with an increase in Li deficiency, which indicates that $Er_{Li}^{\cdot}$ is compensated by lithium vacancies.[8,70] This is based on the fact that for congruent $LiNbO_3$, lithium vacancies already exist in the material.[55,71] Therefore, it is much easier for Er^{3+} to occupy a vacant site. The DFT calculations predicted that under Nb_2O_5-rich conditions, which includes ambient temperature and oxygen partial pressure, the dominant defects are $Er_{Li}^{\cdot}$ compensated by $V_{Li}^{\prime}$ based on the formation energies, which provides theoretical support to this conjecture. It could also explain the observation that increasing the Er concentration tends to increase the Li deficiency in the crystal.

(iv) No direct observation for $Er_{Nb}^{\prime\prime}$ has been reported, although ion-beam channeling indicates that Er may occupy a Nb site[20] and electron paramagnetic resonance (EPR) indicates Er sits on both Li and Nb sites.[72] This absence may be partially due to the methods to incorporate the Er ions into the crystal. The Er^{3+} doping is often achieved during Czochralski growth or diffusion doping,[6] the latter involving the diffusion of Er ions into congruent $LiNbO_3$. It has been reported that the diffusion of Er^{3+} is through the Li sublattice.[73,74] The diffusion of Nb was also found to be much slower than that of lithium vacancies.[73,75,76] Therefore, it is probably much easier for an Er ion to move into a Li sublattice and stay there rather than to push Nb ions off their lattice sites during these kinetic processes; this would make the incorporation of Er on a Nb site difficult.

Furthermore, both Czochralski growth and diffusion doping predetermine the dominant defects to Er on Li site compensated by lithium vacancies. These existing defects can be expected to play a significant role when the sample is converted to the stoichiometric composition using VTE under Li_2O-rich conditions. Taking nearly stoichiometric $Li_{0.498}Nb_{0.5+x}O_3$, for example, after VTE process, the concentration of lithium vacancy is still 0.4%. If we assume that the lithium vacancies are primarily compensated by $Er_{Li}^{\cdot}$, 0.2% of $Er_{Li}^{\cdot}$ would be required. The system would thus be equivalent to 0.2 mol % $Er:LiNbO_3$. Since the concentration of $Er_{Li}^{\cdot}$ and $Er_{Nb}^{\prime\prime}$ is a constant, the concentration $Er_{Nb}^{\prime\prime}$ of can be calculated using

$$[Er_{Li}^{\cdot\cdot\cdot}][Er_{Nb}^{\prime\prime}] = \exp(-\Delta G_f/kT), \tag{3}$$

where, ΔG_f is the defect formation energy, k is the Boltzmann constant, and T is the temperature in Kelvin. At room temperature, the concentration of $Er_{Nb}^{\prime\prime}$ is estimated to be 9.7×10^{-26}, which is ~23 orders of magnitude smaller than $Er_{Li}^{\cdot}$. Increasing the temperature will increase the concentration of $Er_{Nb}^{\prime\prime}$, such that at 800 K, the concentration of $Er_{Nb}^{\prime\prime}$ is calculated to be 1.01×10^{-5}. However, this is still 2 orders of magnitude smaller than the concentration of $Er_{Li}^{\cdot}$. Thus, compared to the concentration of $Er_{Li}^{\cdot}$, the $Er_{Nb}^{\prime\prime}$ concentration is negligible. These calculations indicate that even a small lithium vacancy concentration could significantly affect the defect chemistry of the system. Furthermore, it may provide an explanation of why the Er on Nb site has not been observed.

V. CONCLUSIONS

First principles calculations have been used to characterize the structure and energetics of Er defects and defect clusters in $LiNbO_3$. The formation energies of various types of defects have been calculated and the dominant defects,

which are those with the lowest DFEs, have been determined for both Li_2O-rich and Nb_2O_5-rich conditions. It was found that under both conditions Er primarily sits on the Li site, which is consistent with the experimental site selective spectroscopy measurements. Furthermore, several slightly different microstructural environments of the Er^{3+} ions have been analyzed based on arrangements of $Er_{Li}^{\cdot}$ with other point defects.

The charge compensation mechanism has been predicted to be lithium vacancies under Nb_2O_5-rich conditions and Er^{3+} on a niobium site under Li_2O-rich conditions, which is consistent with an earlier conjecture, although there has been no direct observation of Er''_{Nb}. The method to incorporate Er into $LiNbO_3$ using Czochralski growth or diffusion doping is considered to be the reason, as these processes predetermine the dominant defects to be Er on Li site compensated by lithium vacancies. Small amount of lithium vacancies (0.4%) could significantly affect the defect chemistry when the sample is converted to stoichiometric composition using VTE under Li_2O-rich conditions, which leads to a negligible concentration of Er on Nb site.

ACKNOWLEDGMENTS

This work is supported by the National Science Foundation under Grants No. DMR-0602986 and No. DMR-0303279. The computation resources are provided by the high performance center (HPC) at University of Florida and Florida Laboratory for Advanced Materials Engineering Simulation (FLAMES).

*Corresponding author; sphil@mse.ufl.edu

[1] K. K. Wong, *Properties of Lithium Niobate* (INSPEC, Stevenage, Herts, UK, 2002).
[2] V. Gopalan, V. Dierolf, and D. A. Scrymgeour, Annu. Rev. Mater. Res. **37**, 449 (2007).
[3] D. M. Gill, J. C. Wright, and L. Mccaughan, Appl. Phys. Lett. **64**, 2483 (1994).
[4] H. Suche, R. Wessel, S. Westenhofer, W. Sohler, S. Bosso, C. Carmannini, and R. Corsini, Opt. Lett. **20**, 596 (1995).
[5] J. G. Sole, L. Bausa, D. Jaque, E. Montoya, H. Murrieta, and F. Jaque, Spectrochim. Acta, Part A **54**, 1571 (1998).
[6] I. Baumann, R. Brinkmann, M. Dinand, W. Sohler, L. Beckers, C. Buchal, M. Fleuster, H. Holzbrecher, H. Paulus, K. H. Muller, T. Gog, G. Materlik, O. Witte, H. Stolz, and W. von der Osten, Appl. Phys. A: Mater. Sci. Process. **64**, 33 (1997).
[7] V. Dierolf, C. Sandmann, A. B. Kutsenko, and T. Troster, Radiat. Eff. Defects Solids **155**, 253 (2001).
[8] V. Dierolf and C. Sandmann, J. Lumin. **125**, 67 (2007).
[9] S. Balsamo, S. Maio, I. Montrosset, H. Suche, and W. Sohler, Opt. Quantum Electron. **31**, 29 (1999).
[10] I. Baumann, S. Bosso, R. Brinkmann, R. Corsini, M. Dinand, A. Greiner, K. Schafer, J. Sochtig, W. Sohler, H. Suche, and R. Wessel, IEEE J. Sel. Top. Quantum Electron. **2**, 355 (1996).
[11] J. Amin, J. A. Aust, D. L. Veasey, and N. A. Sanford, Electron. Lett. **34**, 456 (1998).
[12] V. Voinot, R. Ferriere, and J. P. Goedgebuer, Electron. Lett. **34**, 549 (1998).
[13] V. Dierolf, T. Morgus, C. Sandmann, E. Cantelar, F. Cusso, P. Capek, J. Spirkova, K. Polgar, W. Sohler, and A. Ostendorf, Radiat. Eff. Defects Solids **158**, 263 (2003).
[14] V. Dierolf, C. Sandmann, S. Kim, V. Gopalan, and K. Polgar, J. Appl. Phys. **93**, 2295 (2003).
[15] V. Dierolf, C. Sandmann, V. Gopalan, S. Kim, and K. Polgar, Radiat. Eff. Defects Solids **158**, 247 (2003).
[16] T. Gog, M. Griebenow, and G. Materlik, Phys. Lett. A **181**, 417 (1993).
[17] T. Gog, T. Harasimowicz, B. N. Dev, and G. Materlik, Europhys. Lett. **25**, 253 (1994).
[18] L. Kovacs, L. Rebouta, J. C. Soares, M. F. Dasilva, M. Hageali, J. P. Stoquert, P. Siffert, C. Zaldo, Z. Szaller, and K. Polgar, Mater. Sci. Eng., B **9**, 505 (1991).
[19] C. Prieto and C. Zaldo, Solid State Commun. **83**, 819 (1992).
[20] L. Rebouta, M. F. daSilva, J. C. Soares, D. Serrano, E. Dieguez, F. Agullo Lopez, and J. Tornero, Appl. Phys. Lett. **70**, 1070 (1997).
[21] T. Nolte, T. Pawlik, and J. M. Spaeth, Solid State Commun. **104**, 535 (1997).
[22] D. M. Gill, L. McCaughan, and J. C. Wright, Phys. Rev. B **53**, 2334 (1996).
[23] O. Witte, H. Stolz, and W. von der Osten, J. Phys. D **29**, 561 (1996).
[24] S. Erdei and V. T. Gabrieljan, Cryst. Res. Technol. **24**, 987 (1989).
[25] H. L. Wang, Y. Hang, J. Xu, L. H. Zhang, S. N. Zhu, and Y. Y. Zhu, Mater. Lett. **58**, 3119 (2004).
[26] F. S. Chen, J. Appl. Phys. **40**, 3389 (1969).
[27] R. L. Holman, *Processing of Crystalline Ceramics* (Plenum, New York, 1978).
[28] R. J. Holmes and D. M. Smyth, J. Appl. Phys. **55**, 3531 (1984).
[29] R. M. Araujo, K. Lengyel, R. A. Jackson, L. Kovacs, and M. E. G. Valerio, J. Phys.: Condens. Matter **19**, 046211 (2007).
[30] P. Hohenberg and W. Kohn, Phys. Rev. **136**, B864 (1964).
[31] W. Kohn and L. J. Sham, Phys. Rev. **140**, A1133 (1965).
[32] G. Kresse and J. Furthmuller, Comput. Mater. Sci. **6**, 15 (1996).
[33] G. Kresse and J. Furthmuller, Phys. Rev. B **54**, 11169 (1996).
[34] P. E. Blochl, Phys. Rev. B **50**, 17953 (1994).
[35] P. Blaha, K. Schwarz, P. Sorantin, and S. B. Trickey, Comput. Phys. Commun. **59**, 399 (1990).
[36] D. Vanderbilt, Phys. Rev. B **41**, 7892 (1990).
[37] Q. K. Li, B. Wang, C. H. Woo, H. Wang, and R. Wang, J. Phys. Chem. Solids **68**, 1336 (2007).
[38] H. J. Monkhorst and J. D. Pack, Phys. Rev. B **13**, 5188 (1976).
[39] A. M. Boring and J. L. Smith, Challenges in Plutonium Science **1**, 91 (2000).
[40] K. T. Moore and G. van der Laan, Rev. Mod. Phys. **81**, 235 (2009).
[41] U. von Barth and C. D. Gelatt, Phys. Rev. B **21**, 2222 (1980).
[42] A. Kiejna, G. Kresse, J. Rogal, A. De Sarkar, K. Reuter, and M. Scheffler, Phys. Rev. B **73**, 035404 (2006).
[43] J. Hafner, J. Comput. Chem. **29**, 2044 (2008).

[44] T. Oguchi, K. Terakura, and A. R. Williams, Phys. Rev. B **28**, 6443 (1983).
[45] M. Cococcioni and S. de Gironcoli, Phys. Rev. B **71**, 035105 (2005).
[46] S. L. Dudarev, G. A. Botton, S. Y. Savrasov, C. J. Humphreys, and A. P. Sutton, Phys. Rev. B **57**, 1505 (1998).
[47] A. I. Liechtenstein, V. I. Anisimov, and J. Zaanen, Phys. Rev. B **52**, R5467 (1995).
[48] C. G. Van de Walle, P. J. H. Denteneer, Y. Bar-Yam, and S. T. Pantelides, Phys. Rev. B **39**, 10791 (1989).
[49] S. G. Louie, M. Schluter, J. R. Chelikowsky, and M. L. Cohen, Phys. Rev. B **13**, 1654 (1976).
[50] W. E. Pickett, K. M. Ho, and M. L. Cohen, Phys. Rev. B **19**, 1734 (1979).
[51] C. G. Van de Walle and J. Neugebauer, J. Appl. Phys. **95**, 3851 (2004).
[52] K. Reuter and M. Scheffler, Phys. Rev. B **65**, 165403 (2002).
[53] A. F. Kohan, G. Ceder, D. Morgan, and C. G. Van de Walle, Phys. Rev. B **61**, 15019 (2000).
[54] J. He, R. K. Behera, M. W. Finnis, X. Li, E. C. Dickey, S. R. Phillpot, and S. B. Sinnott, Acta Mater. **55**, 4325 (2007).
[55] H. X. Xu, D. Lee, J. He, S. B. Sinnott, V. Gopalan, V. Dierolf, and S. R. Phillpot, Phys. Rev. B **78**, 174103 (2008).
[56] R. DeHoff, *Thermodynamics in Materials Science* (Taylor & Francis Group, Boca Raton, FL, 2006).
[57] R. Xu, Y. Y. Zhu, S. Chen, F. Xue, Y. L. Fan, X. J. Yang, and Z. M. Jiang, J. Cryst. Growth **277**, 496 (2005).
[58] R. M. Moon, W. C. Koehler, H. R. Child, and L. J. Raubenheimer, Phys. Rev. **176**, 722 (1968).
[59] D. Redfield and W. J. Burke, J. Appl. Phys. **45**, 4566 (1974).
[60] A. Dhar and A. Mansingh, J. Appl. Phys. **68**, 5804 (1990).
[61] J. P. McKelvey, *Solid State Physics For Engineering and Materials Science* (Krieger Publishing Company, Malabar, Florida, 1993).
[62] R. D. Shannon, Acta Crystallogr., Sect. A: Cryst. Phys., Diffr., Theor. Gen. Crystallogr. **32**, 751 (1976).
[63] A. Mehta, E. K. Chang, and D. M. Smyth, J. Mater. Res. **6**, 851 (1991).
[64] T. K. Halstead, J. Chem. Phys. **53**, 3427 (1970).
[65] M. W. Barsoum, *Fundamentals of Ceramics* (Taylor & Francis, Bodmin, Cornwall, UK, 2002).
[66] B. Hourahine, S. Sanna, B. Aradi, C. Kohler, and T. Frauenheim, Physica B **376-377**, 512 (2006).
[67] A. Lazreg, Z. Dridi, F. Benkabou, and B. Bouhafs, Physica B **403**, 2702 (2008).
[68] M. Losurdo, M. M. Giangregorio, P. Capezzuto, G. Bruno, R. G. Toro, G. Malandrino, I. L. Fragala, L. Armelao, D. Barreca, E. Tondello, A. A. Suvorova, D. Yang, and E. A. Irene, Adv. Funct. Mater. **17**, 3607 (2007).
[69] D. M. B. P. Milori, I. J. Moraes, A. C. Hernandes, R. R. Desouza, M. S. Li, M. C. Terrile, and G. E. Barberis, Phys. Rev. B **52**, 3802 (1995).
[70] K. Polgar and A. P. Skvortsov, Radiat. Eff. Defects Solids **150**, 287 (1999).
[71] J. Blumel, E. Born, and T. Metzger, J. Phys. Chem. Solids **55**, 589 (1994).
[72] S. Y. Wu and W. C. Zheng, Phys. Rev. B **65**, 224107 (2002).
[73] D. P. Birnie, J. Mater. Sci. **28**, 302 (1993).
[74] C. Buchal and S. Mohr, J. Mater. Res. **6**, 134 (1991).
[75] V. B. Ptashnik, T. Y. Dunaeva, and I. V. Myasnikov, Inorg. Mater. **21**, 1814 (1985).
[76] V. I. Lapshin and A. P. Rumyantsev, Inorg. Mater. **12**, 1797 (1976).